nature communications

Article

https://doi.org/10.1038/s41467-025-56102-7

# Bilayer electrified-membrane with pair-atom tin catalysts for near-complete conversion of low concentration nitrate to dinitrogen

Received: 19 July 2024

Accepted: 6 January 2025

Published online: 28 January 2025

Check for updates

Xuanhao Wu[1,2], Xiaoxiong Wang[3] ✉, Yunshuo Wu[1], Huimin Xu[1], Zhe Li[1], Rongrong Hong[1], Kali Rigby[2], Zhongbiao Wu[1] & Jae-Hong Kim[2,4] ✉

Discharge of wastewater containing nitrate ($NO_3^-$) disrupts aquatic ecosystems even at low concentrations. However, selective and rapid reduction of $NO_3^-$ at low concentration to dinitrogen ($N_2$) is technically challenging. Here, we present an electrified membrane (EM) loaded with Sn pair-atom catalysts for highly efficient $NO_3^-$ reduction to $N_2$ in a single-pass electrofiltration. The pair-atom design facilitates coupling of adsorbed N intermediates on adjacent Sn atoms to enhance $N_2$ selectivity, which is challenging with conventional fully-isolated single-atom catalyst design. The EM ensures sufficient exposure of the catalysts and intensifies the catalyst interaction with $NO_3^-$ through mass transfer enhancement to provide more N intermediates for $N_2$ coupling. We further develop a reduced titanium dioxide EM as the anode to generate free chlorines for fully oxidizing the residual ammonia (<1 mg-N $L^{-1}$) to $N_2$. The sequential cathode-to-anode electrofiltration realizes near-complete removal of 10 mg-N $L^{-1}$ $NO_3^-$ and ~100% $N_2$ selectivity with a water resident time on the order of seconds. Our findings advance the single-atom catalyst design for $NO_3^-$ reduction and provide a practical solution for $NO_3^-$ contamination at low concentrations.

Nitrate ($NO_3^-$) contamination resulting from the discharge of inadequately treated wastewater disrupts aquatic ecosystems through eutrophication followed by harmful algal blooms[1]. The algal blooms can be triggered by $NO_3^-$ at a concentration as low as 1 mg-N $L^{-1}$ [2], therefore, underscoring the need for water treatment systems to remove $NO_3^-$ with low concentrations[3]. However, near-complete removal of $NO_3^-$ at low concentrations in complex water matrices is difficult and costly. Electrocatalytic $NO_3^-$ reduction reaction ($NO_3RR$) to dinitrogen ($N_2$) or ammonia ($NH_3$) offers a promising alternative to be applied for $NO_3^-$ removal from water. Electrochemical processes offer advantages including rapid reaction kinetics, adaptability to various treatment scenarios, the potential to be modularized for decentralized application, and minimal generation of secondary wastes such as sludges or concentrates[4,5].

Numerous electrocatalysts have been developed for $NO_3RR$ towards $NH_3$ instead of $N_2$ with the goal of resource recovery[6–9]. However, the practicability of $NH_3$ recovery from low concentration $NO_3^-$ remains questionable, considering the complexity and high cost of separating dilute $NH_3$ from water[10]. It is noteworthy that $NH_3$ can be even more toxic compared to $NO_3^-$[11], posing higher environmental risks. Therefore, developing $NO_3RR$ systems that can completely convert low-concentration $NO_3^-$ to $N_2$ with close to 100% selectivity is yet to be developed. Conventionally, $NO_3^-$ reduction to $N_2$ requires a precious noble metal[12,13] in combination with a promoter metal (e.g., Cu) to improve the adsorption and charge transfer of the reactants and

[1]Department of Environmental Engineering, Zhejiang University, Hangzhou, China. [2]Department of Chemical and Environmental Engineering, Yale University, New Haven, CT, USA. [3]Institute for Ocean Engineering & Center of Double Helix & Shenzhen Key Laboratory of Advanced Technology for Marine Ecology, Tsinghua Shenzhen International Graduate School, Tsinghua University, Shenzhen, China. [4]School of Civil, Environmental and Architectural Engineering, Korea University, 145 Anam-ro, Seongbuk-gu, Seoul, Republic of Korea. ✉e-mail: wang.xiaoxiong@sz.tsinghua.edu.cn; jaehong.kim@yale.edu

intermediates. However, the limited availability and high cost of the noble metals restrict their application for $NO_3RR$[14].

Single-atom catalysts (SACs) have emerged as a transformative alternative in catalyst material design. With close to 100% atomic efficiency, SACs expose more active surface sites than nanoparticle counterparts, offering unparalleled efficiency and selectivity in various catalytic schemes[15]. The strong interaction of SACs with the support via surface defects and N-atomic anchors also offers enhanced chemical stability[16–18]. Despite these advantages, the spatial isolation of catalytic sites in SAC architecture is not considered ideal for $NO_3RR$ toward $N_2$. With fully isolated SACs, the *N intermediate generated on each SAC site cannot easily interact with another *N to undergo the *N-*N coupling step, which is critical for $N_2$ generation[8,19,20]. This is the reason that most reported SACs are prone to promote the $NH_3$ selectivity through *N-*H coupling[21–25]. (Fig. 1, left panel).

In this study, we propose a viable SAC architecture, pairs of tin (Sn) single atoms, to enhance the $NO_3RR$ selectivity toward $N_2$ production (Fig. 1, right panel). Closely-spaced dual active sites intend to facilitate *N-*N coupling that are favored in multi-atom catalytic sites[26]. Sn is selected because of its rapid $NO_3RR$ kinetics and high $N_2$ selectivity[27,28]. We incorporate Sn pair-atoms in an innovative electrified membrane (EM) to ensure their exposure in the membrane nanopores. The EM intensifies the catalyst interaction with $NO_3^-$ during flow-through operation[29–32], overcoming the mass transfer limitation of the conventional plate electrodes[33,34] and providing more *N sources for $N_2$ coupling[35–37]. We demonstrate highly efficient conversion of low concentration $NO_3^-$ (10 mg-N $L^{-1}$) to $N_2$ in a single-pass filtration through the Sn pair-atom-loaded EM. We further incorporate a reduced titanium dioxide ($TiO_{2-x}$) EM anodic bottom layer to generate free chlorines from chloride ion ($Cl^-$) in water to fully oxidize the residual ammonia ($NH_3$) downstream (<1 mg-N $L^{-1}$) into $N_2$.

## Results

### Synthesis and characterization of Sn single-atom catalysts

We loaded Sn single atoms on carbon black (CB) support using a ligand-mediated method (Fig. 2a)[38]. In brief, the $Sn^{4+}$ complex with 1,10-phenanthroline (Phen) at a molar ratio of $Sn^{4+}$:Phen = 1:3 was adsorbed onto CB at target Sn loading of 1 and 5 wt%. Subsequent annealing in Ar atmosphere at 600 °C for 3 h produced N-doped carbon black (NCB)-supported Sn SACs. Transmission electron microscopy (TEM) images showed the porous structure of NCB and confirmed the absence of nanoparticles (Fig. S1). Aberration-corrected high-angle annular dark field-scanning transmission electron microscopy (AC HAADF-STEM) images suggested the atomic dispersion of Sn atoms on NCB. At the target Sn loading of 5%, we predominantly observed pair-atom sites (i.e., two single atoms placed close to each other, denoted as $Sn_2$/NCB, Fig. 2b). In contrast, fully-isolated Sn single-atom sites became more dominant over pair-atom sites at 1 wt% Sn loading (denoted as $Sn_1$/NCB) (Fig. 2c). The formation of Sn pair-atoms may attribute to the generation of Phen-$Sn^{4+}$ precursor binuclear complexes in a distorted trigonal bipyramidal configuration in the solution[39–41]. In addition, increasing the density of single atoms on the substrate to tune their site-to-site distance can create correlating atomic interactions between neighboring single atom sites[42,43]. When the dispersed single atoms are close enough in catalysts with a $M_1$–N–C structure ($M_1$ represents metal single atom), a strong interaction could occur between the two adjacent single atoms to form a double active center to improve the catalytic performance[43]. However, increasing only the density of single atoms to create pair-atom sites cannot precisely control the coordination configuration and distribution uniformity compared to methods such as the metal binuclear precursor deposition[44,45]. Therefore, both Sn pair-atom and single-atom sites were observed, yet the composition of the former was dominant with the increase of Sn loading. The energy dispersion spectroscopy (EDS) mapping of $Sn_2$/NCB confirmed the uniform dispersion of Sn on the NCB support (Fig. 2d). Statistical image analysis determined the averaged distance between Sn atoms in $Sn_2$/NCB at $d = 4.8 \pm 0.7$ Å (Fig. 2e–g). We also confirmed the mass loading to be within 4% error from the target, using inductively coupled plasma-mass spectrometry (ICP-MS) analysis.

X-ray diffraction (XRD) patterns of $Sn_2$/NCB and NCB showed similar broad peaks at 25° and 44° after pyrolysis (Fig. S2), indicating

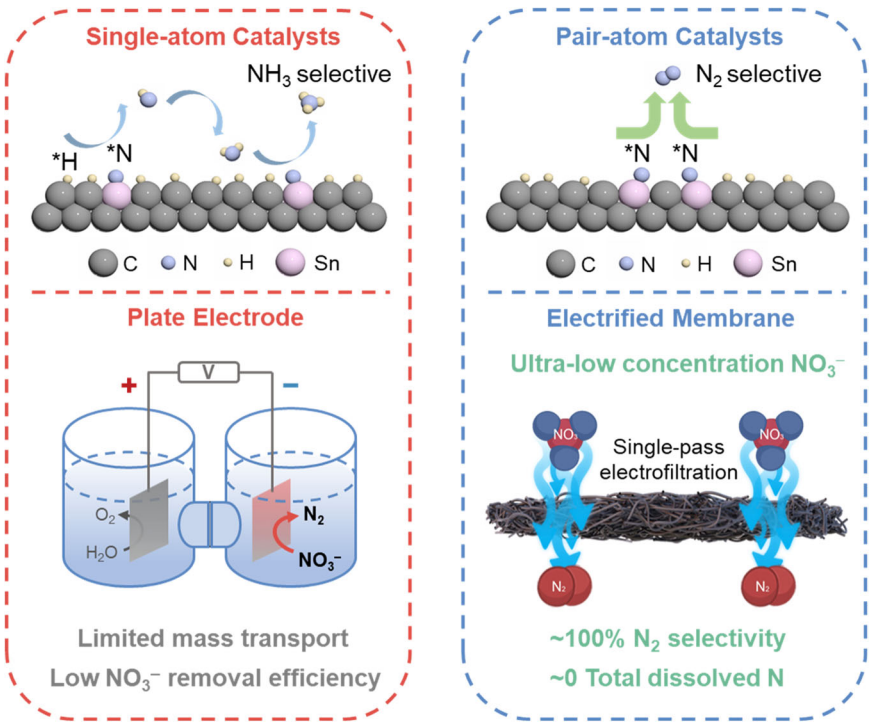


**Fig. 1 | Design principles of this work.** Schematic illustrating the design principles of incorporating single-atom catalysts in traditional plate electrode (left panel) or pair-atom catalysts in an electrified membrane for realizing near-complete conversion of low concentration nitrate to dinitrogen (right panel).

https://doi.org/10.1038/s41467-025-56102-7

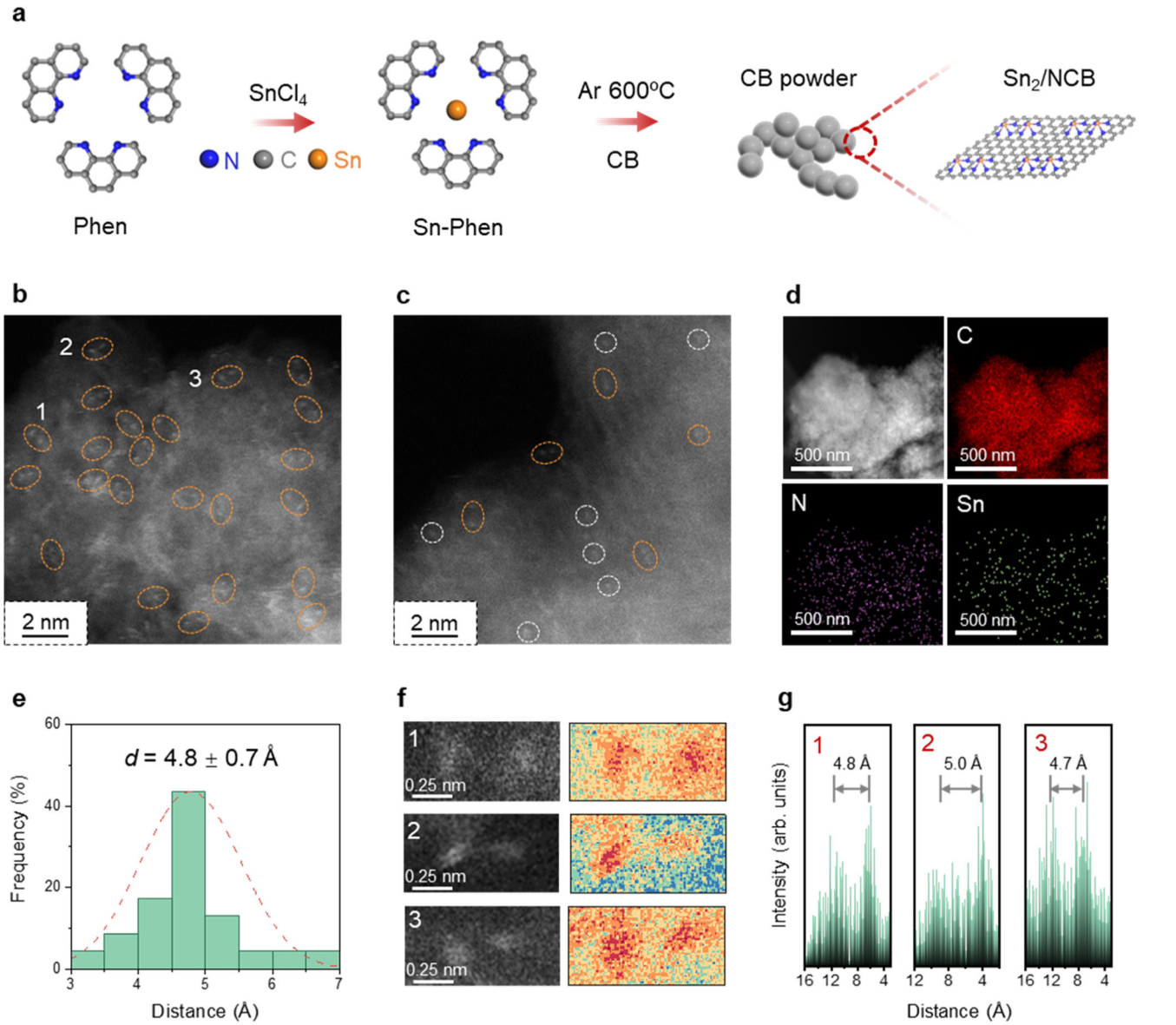


**Fig. 2 | Characterization of $Sn_2$/NCB. a** Schematics of synthesis procedures of $Sn_2$/NCB. **b** AC HAADF-STEM image of $Sn_2$/NCB. **c** AC HAADF-STEM image of $Sn_1$/NCB. **d** TEM EDS mapping images of $Sn_2$/NCB. **e** Histogram of the distribution of distances between Sn pair-atoms. Three representative Sn pair-atoms sites: **f** enlarged AC HAADF-STEM images and surface intensity plots; **g** the variation in brightness along the Sn pair-atoms. Source data are provided as a Source Data file.

poor crystallinity of carbon. XRD analysis also confirmed the absence of metal nanoparticles. In Raman analysis, the relative intensity ratio between the D and G bands ($I_D/I_G$) of $Sn_2$/NCB and NCB were 1.01 and 1.02 respectively, higher than the 0.99 of pure NCB (Fig. S3), consisting of the increased surface defects due to nitrogen doping[46]. X-ray photoelectron spectroscopy (XPS) of $Sn_2$/NCB also confirmed the absence of characteristic $Sn^0$ peak at ~485.0 eV[47]. XPS analysis further suggested that the binding energies of two Sn 3d peaks at 487.3 eV and 497.3 eV were close to the values reported for $Sn^{4+}$ (Fig. S4a)[47]. The N 1s spectrum showed the presence of pyridinic N (399.0 eV), Sn–N (400.0 eV), pyrrolic N (400.8 eV), and graphitic N (401.5 eV) (Fig. S4b)[48].

We further examined the oxidation state and coordination environment of Sn in $Sn_2$/NCB using X-ray adsorption (XAS) spectroscopy. The X-ray absorption near edge structure (XANES) spectrum at Sn K-edge shows that the edge energy of $Sn_2$/NCB was in between Sn foil and Sn(IV) phthalocyanine (SnPc) standards (Fig. 3a), suggesting that the oxidation state of Sn in $Sn_2$/NCB ($\delta_2^+$) was $0 < \delta_2^+ < 4^+$. Note that there was a shift towards higher edge energy (eV) from $Sn_2$/NCB to $Sn_1$/NCB (Fig. 3b). The lower edge energy suggests that Sn pair-atoms would be in a more reduced state compared to single atoms (i.e., $\delta_2^+ < \delta_1^+$). A similar shift of electron distribution towards clustered single atoms due to the electronic interactions between short-distanced atoms has been observed with neighboring or ensemble single atoms[49,50]. The linear correlation analysis between the edge energy and oxidation state of Sn indicated that the oxidation states of Sn would be around $\delta_2^+ = 2.8$ for $Sn_2$/NCB and $\delta_1^+ = 3.6$ for $Sn_1$/NCB (Fig. 3c).

The Fourier transformed-extended X-ray absorption fine structure (FT-EXAFS) spectra of $Sn_2$/NCB and $Sn_1$/NCB exhibited major peaks at 1.57 Å and 1.58 Å, corresponding to the Sn-N coordination similar to the SnPc standard (Fig. 3d). The $Sn_2$/NCB did not exhibit the peak of Sn-Sn coordination at 2.79 Å of Sn foil, indicating the absence of direct Sn-Sn interactions. The coordination number of Sn pair-atom in $Sn_2$/NCB was estimated to be 4.1 ± 0.2 based on EXAFS fitting (Fig. 3e and Table S1), which suggested the formation of Sn-$N_4$ structure for both pair-atoms. The *k*-space and *R*-space of $Sn_2$/NCB, $Sn_1$/NCB, SnPc, and Sn foil were additionally analyzed via wavelet transform (WT) to obtain 2D and 3D contour maps (Fig. 3f–i). The maximal peak near

https://doi.org/10.1038/s41467-025-56102-7

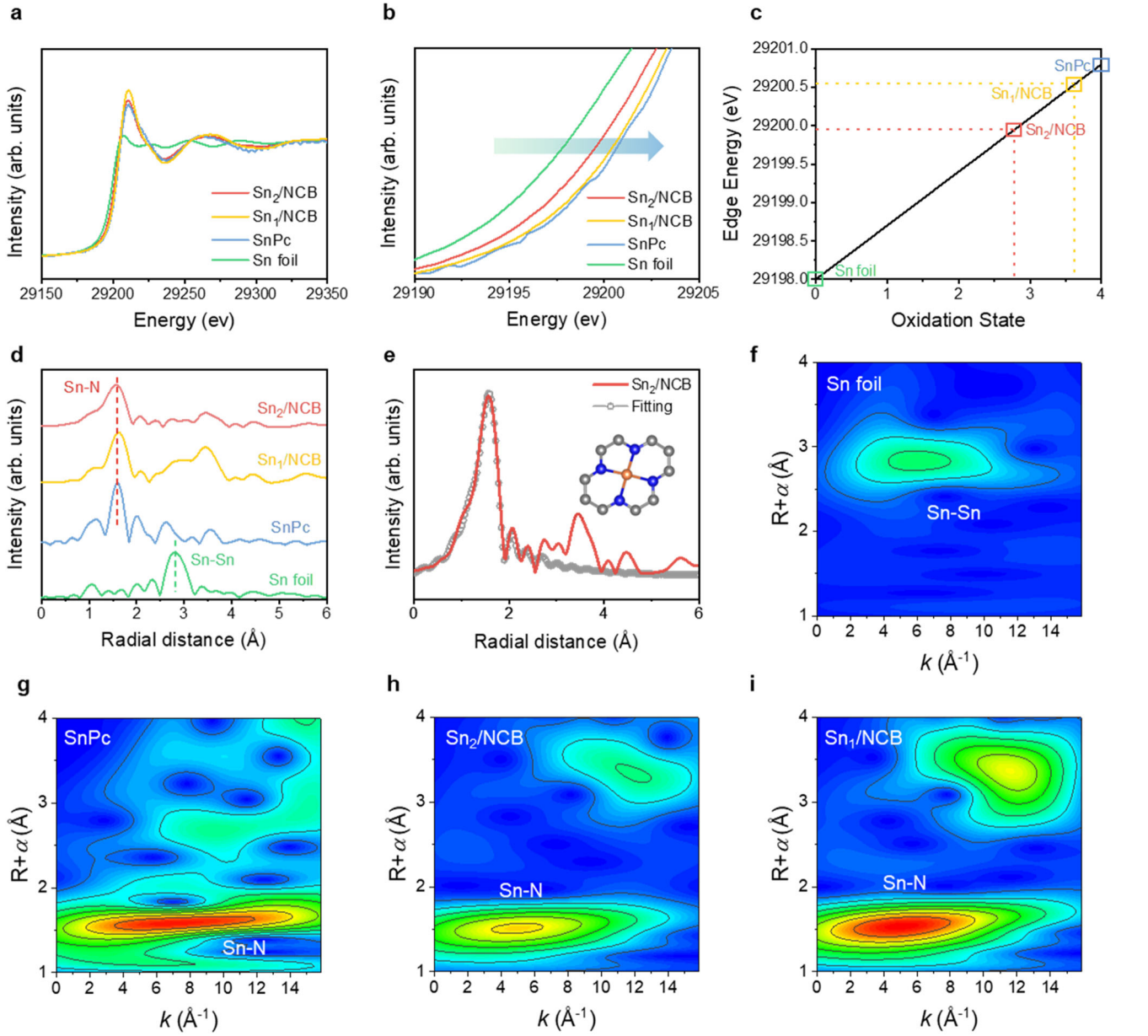


**Fig. 3 | Characterization of $Sn_2$/NCB. a**, **b** Normalized XANES spectra of Sn K-edge. The arrow indicates the rise of oxidation state. **c** The linear correlation between the edge energy (eV) and oxidation state of Sn. **d** FT-EXAFS spectra. **e** FT-EXAFS fitting of $Sn_2$/NCB. Inset: schematic diagram of the Sn-$N_4$ structure. WT-XAFS spectra of (**f**) Sn foil, (**g**) SnPc, (**h**) $Sn_2$/NCB, and (**i**) $Sn_1$/NCB. Source data are provided as a Source Data file.

4.9 $Å^{-1}$ of $Sn_2$/NCB was attributed to the Sn-N bond, which shifted slightly from the 5.2 $Å^{-1}$ of $Sn_1$/NCB. These indicated the differences in the Sn−N coordination in $Sn_2$/NCB due to the coupling compared to fully isolated single-atom sites in $Sn_1$/NCB.

### Performance of $Sn_2$/NCB in $NO_3$RR and mechanistic insights

We first employed a batch cell to evaluate the $NO_3$RR performance of $Sn_2$/NCB. $Sn_2$/NCB showed a higher current density compared to $Sn_1$/NCB and NCB during linear sweep voltammetry (LSV) measurements, indicating its superior $NO_3$RR activity than $Sn_1$/NCB and NCB (Fig. 4a). The $Sn_2$/NCB showed a comparable $NO_3^-$ conversion rate (401.6 mg-N $h^{-1}$ $m^{-2}$) with $Sn_1$/NCB (Fig. 4b). However, $N_2$ selectivity was significantly higher with $Sn_2$/NCB (86%) than $Sn_1$/NCB (50%), consistent with our hypothesis that the Sn pair-atom architecture would be beneficial for enhancing the $N_2$ generation over $NH_3$. $Sn_2$/NCB also exhibited higher $NO_3^-$ conversion rate and $N_2$ selectivity compared to other benchmark Sn materials such as nanocluster (1 wt% and 5 wt%), nanoparticle (10 wt% and 20 wt%), and bulk powder (Fig. S6). These results suggested that the pair-atom structure rather than the Sn loading played a critical role in enhancing the $NO_3$RR performance. When applying $Sn_2$/NCB for $NO_3$RR under varied potentials, the $NO_3^-$ conversion rate gradually increased with higher potentials, while the $N_2$ selectivity started to decline above −1.2 V vs. RHE (Fig. 4c).

In situ attenuated total reflectance surface-enhanced infrared absorption spectroscopy (ATR-SEIRAS) was applied to identify the key N intermediates during $NO_3$RR for $Sn_2$/NCB and $Sn_1$/NCB (Fig. 4d, e). Both groups displayed a negative peak at 1224 $cm^{-1}$ corresponding to the Si−O stretching vibration[51] and a bending vibration mode of $H_2O$ at 1640 $cm^{-1}$ [52]. The peaks at 1330 $cm^{-1}$, 1190 $cm^{-1}$, and 1560 $cm^{-1}$ were assigned to $*NO_3^-$, $*NO_2^-$, and *NO, respectively[53]. For $Sn_1$/NCB, a clear peak at 1460 $cm^{-1}$ from the stretching vibration of the N−H bond in $*NH_4^+$ was observed, along with the intermediates including $*NH_2$ at 1140 $cm^{-1}$ and $*NH_2OH$ at 1110 $cm^{-1}$ [52]. A peak at 1030 $cm^{-1}$ corresponded to the generation of $*N_2$[54–56]. In contrast, for $Sn_2$/NCB, the

https://doi.org/10.1038/s41467-025-56102-7

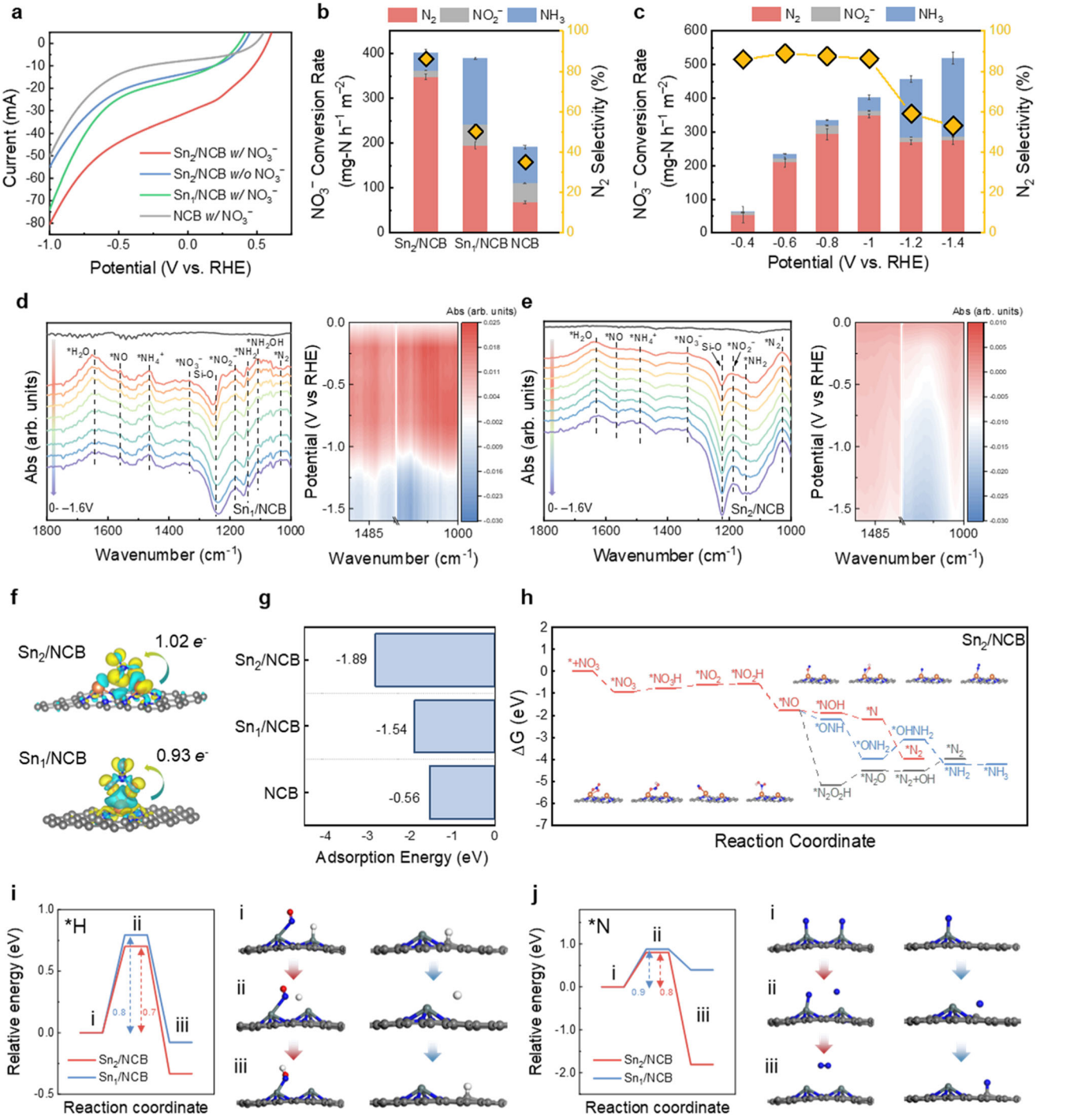


**Fig. 4 | Performance of $Sn_2$/NCB in $NO_3$RR and mechanisms. a** LSV curves of $Sn_2$/NCB with and without $NO_3^-$, $Sn_1$/NCB with $NO_3^-$, and NCB with $NO_3^-$. The voltages were not iR corrected. **b** $NO_3^-$ conversion rates and $N_2$ selectivity of $Sn_2$/NCB, $Sn_1$/NCB, and NCB. **c** $NO_3^-$ conversion rates and $N_2$ selectivity of $Sn_2$/NCB under varied potentials. The voltages were not iR corrected (electrode surface area = 1 $cm^2$, resistance value = 3 Ω). The data in (**b**) and (**c**) are presented as mean values ± s.d. ($n$ = 3). In situ ATR-SEIRAS and the corresponding contour maps of (**d**) $Sn_1$/NCB and (**e**) $Sn_2$/NCB during $NO_3$RR. **f** The charge density difference plots of $NO_3^-$ on $Sn_2$/NCB and $Sn_1$/NCB. **g** The adsorption energies of $NO_3^-$ on CB, NCB, $Sn_1$/NCB, and $Sn_2$/NCB. **h** Gibbs free energy curves of $NO_3^-$ reduction on $Sn_2$/NCB. The inset molecular structures represent the most thermodynamically favorable $N_2$ generation path on $Sn_2$/NCB. Transition state energy diagrams of (**i**) *H and (**j**) *N spillover on $Sn_2$/NCB and $Sn_1$/NCB. Red, blue, white, and grey atoms represent O, N, H, and C elements respectively. Source data are provided as a Source Data file.

peak intensity of $*NH_4^+$ at 1460 $cm^{-1}$ along with other intermediates for $NH_3$ production decreased significantly compared to $Sn_1$/NCB, which was also observed from the corresponding contour maps. Further, the peak intensity of $*N_2$ at 1030 $cm^{-1}$ was more prominent, indicating that $Sn_2$/NCB promoted the conversion of $NO_3^-$ to $N_2$ over $NH_3$ compared to $Sn_1$/NCB.

We further performed density functional theory (DFT) calculations to scrutinize the mechanisms of the enhanced $N_2$ selectivity on Sn pair-atoms over single-atoms. We first evaluated the adsorption strength and charge transfer of $NO_3^-$ on different substrates. The adsorption configurations of $NO_3^-$ on $Sn_1$/NCB and $Sn_2$/NCB were optimized and shown in Fig. S7. Instead of the conventional vertical adsorption configuration on

Sn single-atom, on $Sn_2$/NCB, $NO_3^-$ interacted with two adjacent Sn pair-atoms, with an inclined omega angle (N-Sn-$O_2$-$O_1$) of 87.1°. The coordinates of all atoms in the $NO_3^-$ adsorbed $Sn_1$/NCB and $Sn_2$/NCB models were presented in Supplementary Data 1. The charge density difference plots of $NO_3^-$ on NCB, $Sn_1$/NCB, and $Sn_2$/NCB (Figs. 4f, S8) indicated that the charge transfer from Sn pair-atoms to $NO_3^-$ (1.02 $e^-$) was more significant than Sn single-atoms (0.93 $e^-$). The adsorption of $NO_3^-$ on $Sn_2$/NCB and $Sn_1$/NCB was predominantly chemical adsorption, with adsorption energies of –1.54 eV and –1.89 eV, respectively (Fig. 4g), confirming the adsorption of $NO_3^-$ on $Sn_2$/NCB was stronger than that on $Sn_1$/NCB. The projected density of states (PDOS) diagram showed that after $Sn_1$ introduction, the band gap decreased from 0.68 eV of NCB to 0.23 eV of $Sn_1$/NCB (Fig. S9). After further adding Sn atom to form $Sn_2$/NCB, the contribution of the electronic peak was more obvious, and the band gap was further reduced to 0.14 eV, which would enhance the charge transfer across the catalyst. The $Sn_2$/NCB possessed a slightly more positive *d*-band center and consequently a stronger adsorption strength than that of $Sn_1$/NCB.

We further compared the lowest energy $NO_3$RR pathways for $Sn_2$/NCB versus $Sn_1$/NCB (Fig. 4h and Fig. S10) and other control materials (Fig. S11). The reduction of $NO_3^-$ to *NO followed the $NO_3 \rightarrow *NO_3 \rightarrow *NO_3H \rightarrow *NO_2 \rightarrow *NO_2H \rightarrow *NO$ hydrogenation route. For NCB, the weak adsorption of $NO_3^-$ was inconducive to the occurrence of the reaction. Further hydrogenation of *NO followed three pathways, generating *NOH, *ONH, and $*N_2O_2H$, respectively. On $Sn_1$/NCB, the production of *NOH was inhibited by a positive $\Delta G_{max}$ of 1.0 eV. The $N_2$ generation occurred through energetically favorable pathway of $*NO \rightarrow *N_2O_2H \rightarrow *N_2O \rightarrow *N_2 + OH \rightarrow *N_2$. In contrast, the path toward $NH_3$ ($*NO \rightarrow *ONH \rightarrow *ONH_2 \rightarrow *OHNH_2 \rightarrow *NH_2 \rightarrow *NH_3$) only had a small energy barrier of $\Delta G_{max}$ of 0.1 eV from *NO to *ONH. Therefore, both two paths could happen, while the $N_2$ generation was slightly more favorable. This was consistent with the selectivity of 50% for $N_2$ and the selectivity of 38% for $NH_3$ in batch $NO_3$RR tests.

In contrast, the adsorbed $*NO_3$ and $*NO_3H$ interacted with two Sn pair-atoms on $Sn_2$/NCB. Consequently, their free energies were more negative than those in the case of $Sn_1$/NCB. This indicates that the pair-atom interaction is more conducive to the initiation of the $NO_3$RR. For the *NOH, *ONH, and $*N_2O_2H$ pathways, the most thermodynamically favorable route was $*NO \rightarrow *NOH \rightarrow *N \rightarrow *N_2$. The Sn pair-atom design altered the dominant intermediate of $N_2$ generation to *NOH, which contrasts from $*N_2O_2H$ on Sn single-atoms. In comparison, the *ONH path had a $\Delta G_{max}$ of 0.9 eV of $*ONH_2 \rightarrow *OHNH_2$, while the $*N_2O_2H$ path had a $\Delta G_{max}$ of 0.7 eV of $*N_2O_2H \rightarrow *N_2O$, both inhibiting these pathways. The above calculations collectively suggest that Sn pair-atoms would preferentially lead to the production of $N_2$ compared with $NH_3$, consistent with the experimental results.

Finally, we examined the energetics of transition state involving *H and *N spillover, preceding $N_2$ formation. The energy barriers for water dissociation on both $Sn_2$/NCB and $Sn_1$/NCB were similar (Fig. S12). For $Sn_2$/NCB, *H formed on a Sn site could easily migrate and attack the *NO on the adjacent Sn site (Fig. 4i). In contrast, for $Sn_1$/NCB, *H on a Sn atom needed to spillover onto and migrate across NCB support with an energy barrier of >0.8 eV to react with *NO on another distant Sn atom site. This difference accounts for more effective hydrogenation of *NO with $Sn_2$/NCB than $Sn_1$/NCB. The simulation also suggested that the energy barrier of coupling two *N atoms on Sn pair-atoms to form $N_2$ was 0.8 eV (Fig. 4j), which was lower than the diffusion (spillover) barrier (0.9 eV) of *N from a Sn single-atoms to NCB support. These results confirm that efficient $N_2$ formation through *N coupling is due to close proximity of *N atoms placed on neighboring Sn pair-atoms.

## Design principle, fabrication, and characterization of bilayer electrified membrane

Based on $N_2$-selective $NO_3$RR demonstrated in the batch cell, we incorporated the $Sn_2$/NCB onto a bilayer electrified membrane (bilayer-EM) to further improve the $NO_3$RR kinetics and selectivity. As shown in Fig. 5a, the cathodic layer was placed on the top of the flow cell (i.e., toward the influent side) to selectively reduce $NO_3^-$ to $N_2$. The mass transfer of $NO_3^-$ to catalytic sites would be enhanced due to convection across the porous electrode. Through the anodic bottom layer (i.e., placed below the cathode), free chlorines generated in situ would oxidize the small amount of $NH_3$ generated from the cathode to $N_2$[57,58]. This bilayer-EM was designed to achieve sequential cathode-to-anode electrofiltration and to realize near-complete removal of low-concentration $NO_3^-$ with ~100% $N_2$ selectivity.

We prepared a free-standing electrified membrane ($Sn_2$/NCB-EM) that serves as the top layer of the bilayer-EM by coating the $Sn_2$/NCB on the CNT interwoven framework. The membrane was morphologically uniform across the effective membrane area of 12.6 $cm^2$ and mechanically robust as a flow-through electrode (Fig. 5b). The comparison of the top view SEM images between the catalyst-loaded membrane (Fig. 5c) and a control CNT electrified membrane (CNT-EM, Fig. S13) indicated that the CNT interwoven framework was well-coated with the $Sn_2$/NCB. The cross-section SEM images showed a lamellar structure of the membrane with a thickness of 0.15 mm (Fig. 5d). We also prepared a $TiO_{2-x}$ ceramic electrified membrane ($TiO_{2-x}$-EM) that serves as the bottom anodic layer of the bilayer-EM by reducing a $TiO_2$ ceramic membrane in pure $H_2$ atmosphere at 1100 °C (see Fig. S14a for photos of the ceramic membrane before and after reduction). The $TiO_{2-x}$-EM had the same effective membrane area as the $Sn_2$/NCB-EM (Fig. 5e) but exhibited a much rougher surface (Fig. 5f). XPS spectra demonstrated the slight reduction of the $TiO_2$ ceramic membrane to $TiO_{2-x}$ ($x = 0.11$) with the appearance of $Ti^{3+}$ (Figs. 5g, S14b). We finally placed a thin macroporous polyester fabric as a spacer (photo see Fig. S15) between the top and bottom layers to construct the bilayer-EM.

The bilayer-EM was overall hydrophilic (Fig. S16) with the water contact angle of the bottom $TiO_{2-x}$-EM layer of only 9.0°. The $Sn_2$/NCB coat on the CNT framework improved the hydrophilicity of the top $Sn_2$/NCB-EM layer to a low water contact angle of 30.3°. The coating structure reduced the average pore size and the water permeability of the membrane from 31.3 nm and 148 L $m^{-2}$ $h^{-1}$ $bar^{-1}$ (CNT-EM) to 24.9 nm and 77 L $m^{-2}$ $h^{-1}$ $bar^{-1}$ ($Sn_2$/NCB-EM, Fig. 5h, i), respectively. The smaller pore size and lower water permeability demonstrated a dense interwoven nature of the membrane, which was essential to intensify the utilization of the catalysts and the mass transfer of low concentration $NO_3^-$ during electrofiltration. We noted that the water flux of the bilayer-EM was mainly determined by the top $Sn_2$/NCB-EM layer due to its much smaller water permeability compared with the bottom $TiO_{2-x}$-EM layer (Fig. 5i). Additionally, the electrochemical impedance spectroscopy (EIS) amplitudes of the semicircles for both the $Sn_2$/NCB-EM and the $TiO_{2-x}$-EM were only 23 Ω in 10 mM $Na_2SO_4$ solution (Fig. 5j). These results demonstrated the high conductivity of the bilayer-EM for sufficient electron transfer under a relatively low electrolyte concentration.

## Electrochemical $NO_3^-$-to-$N_2$ reduction using bilayer electrified membrane

We evaluated the performance of the bilayer-EM for removing low-concentration $NO_3^-$ (10 mg-N $L^{-1}$) by electrofiltration of neutral feed solutions containing either 10 mM $Na_2SO_4$ or 10 mM NaCl + 5 mM $Na_2SO_4$ (Fig. S17). The loading amount of $Sn_2$/NCB per membrane was first optimized based on $NO_3^-$ removal efficiency in 10 mM $Na_2SO_4$ (Fig. S18). Under a current density of 2.5 mA $cm^{-2}$ and a permeate flow rate of 1.2 mL $min^{-1}$, $NO_3^-$ removal reached 95.3% at 50 mg of $Sn_2$/NCB. Further increase of loading to 100 mg only slightly increased the removal to 96.3%. Therefore, we used 50 mg catalyst loading for further experiments. We compared the $NO_3^-$ reduction performance of a single-layer $Sn_2$/NCB-EM in flow-through mode (Fig. 6a, middle panel) with that of a $Sn_2$/NCB-loaded carbon paper electrode in flow-by mode

https://doi.org/10.1038/s41467-025-56102-7

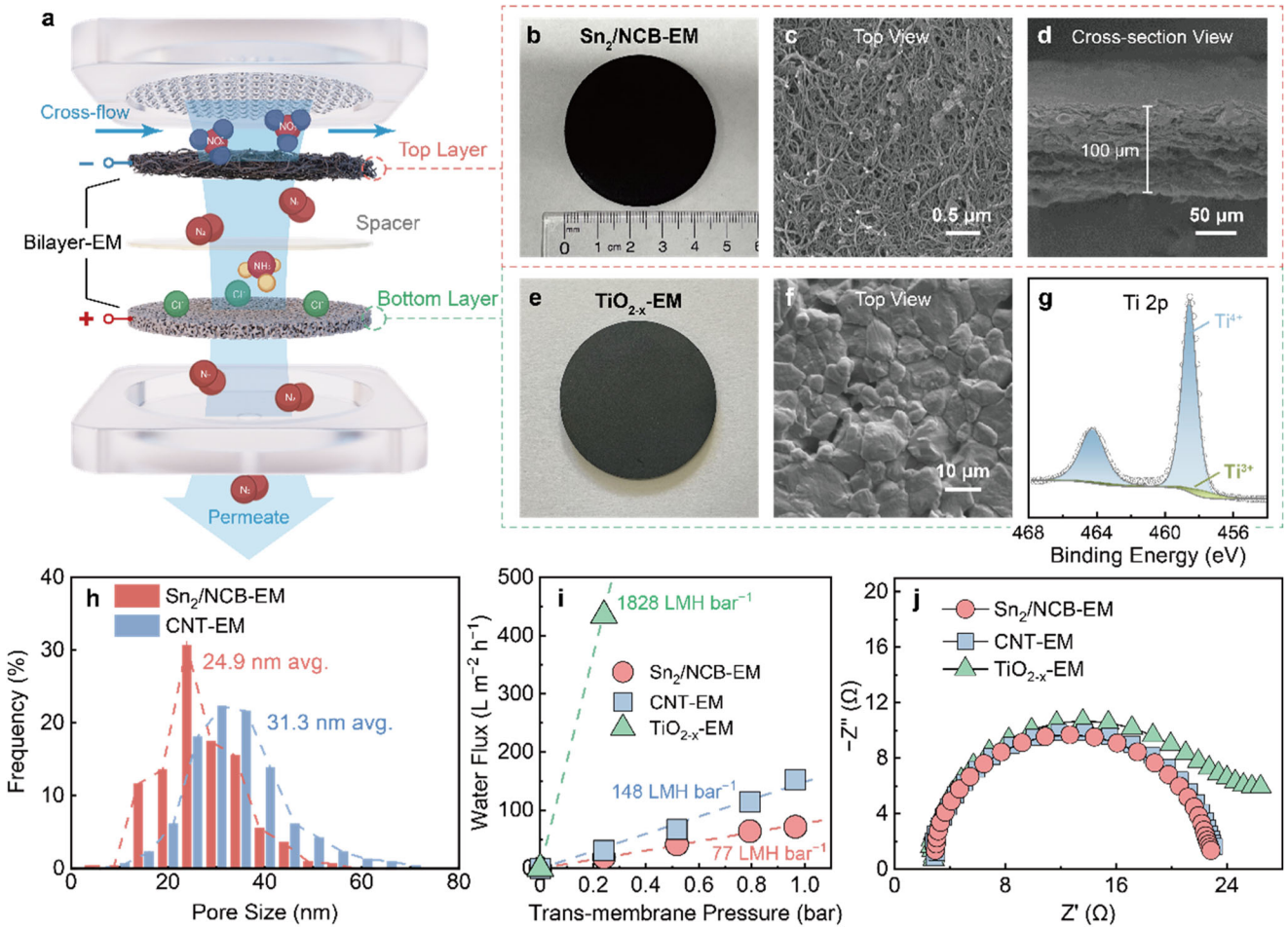


**Fig. 5 | Operating principle and characterization of the bilayer electrified membrane (bilayer-EM). a** Schematic showing the concept of applying the bilayer-EM with sequential cathode-to-anode electrofiltration for realizing near-complete $NO_3^-$-to-$N_2$ reduction with ~100% selectivity. **b** Photograph and SEM images of (**c**) the top and (**d**) the cross-sectional views of the top-layer bilayer-EM (i.e., $Sn_2$/NCB-EM). **e** Photograph, (**f**) top view SEM images, and (**g**) XPS of the bottom-layer bilayer-EM (i.e., $TiO_{2-x}$-EM). **h** Pore size distribution and the average value of the $Sn_2$/NCB-EM and the CNT-EM. **i** Water flux of the $Sn_2$/NCB-EM, the CNT-EM, and the $TiO_{2-x}$-EM. Water permeabilities of the membranes are indicated by the fitted slopes. **j** EIS spectra of the $Sn_2$/NCB-EM, the CNT-EM, and the $TiO_{2-x}$-EM over a frequency range of 1–$10^6$ Hz in 10 mM $Na_2SO_4$ solution. Source data are provided as a Source Data file.

(Fig. 6a, left panel). Under the same current density of 2.5 mA $cm^{-2}$, the $N_2$ selectivity was similar between flow-through (90.1%) and flow-by (89.3%). However, the flow-through mode showed a 3-fold enhancement of $NO_3^-$ conversion rate (546.1 mg-N $h^{-1}$ $m^{-2}$ and 95.3% removal efficiency) compared to that of the flow-by mode (186.3 mg-N $h^{-1}$ $m^{-2}$ and 31.1% removal efficiency), suggesting the significant role of the flow-through system in stimulating mass transfer and reaction kinetics.

We performed computational fluid dynamics (CFD) simulations to examine how flow-through operation enabled more efficient mass transfer and $NO_3^-$ conversion than flow-by mode (Fig. 6b). Flow-through and flow-by modes were simulated considering water flow over a nanofiber interwoven framework and a flat plate, respectively (Fig. S19). The simulated velocity fields showed that the flow of water was significantly intensified inside the nanofiber framework (Fig. S20). Catalysts coated on the framework could increase the thickness of the nanofibers to further enhance the local velocity, resulting in a 12-fold difference in the average velocity fluctuation compared to the plate. This is crucial for improving the utilization efficiency of the highly exposed catalysts coated on the framework. When considering a constant $NO_3^-$ reduction rate at the exposed surface, the $NO_3^-$ concentration decreased rapidly under flow-through mode (Fig. 6$b_1$), whereas the $NO_3^-$ concentration decrease under flow-by mode was moderate (Fig. 6$b_2$). This resulted in a three-time difference in the amount of $NO_3^-$ removal between the flow-through and flow-by modes (Fig. 6$b_3$).

We then applied sequential cathode-to-anode electrofiltration using the bilayer-EM to determine whether the existence of $Cl^-$ could further enhance the selectivity of $N_2$ generation. In the absence of $Cl^-$, similar $NO_3^-$ removal efficiency and $N_2$ selectivity were observed under single-layer (Fig. 6a, middle panel) and bilayer modes (Fig. 6a, right panel). However, when 10 mM $Cl^-$ was added to the feed, the $N_2$ selectivity increased significantly to 97.7% under the bilayer mode (Fig. 6a, right panel). The free chlorine was efficiently generated from electrofiltration of $Cl^-$ through the $TiO_{2-x}$-EM (e.g., 6.7 mg-$Cl_2$ $L^{-1}$ at 2.5 mA $cm^{-2}$, Fig. 6c). The free chlorine or hypochlorous acid (HClO) from chlorine dissolution would oxidize the small amount of $NH_3$ released from the top $Sn_2$/NCB-EM layer into $N_2$[57,58], which resulted in a low residual total nitrogen concentration (the sum of $NO_3^-$, $NO_2^-$, and $NH_3$) of only 0.5 mg-N $L^{-1}$ in the permeate even under the high water treatment capacity of 72 mL $h^{-1}$. We note that our proposed method is suitable only for removing $NH_3$ with low concentrations (<1.5 mg-N $L^{-1}$), considering that free chlorine (dosage of 6–15 mg-$Cl_2$ $L^{-1}$) is generally added in the treated municipal water for disinfection[59,60]. Applying chlorination to oxidize high-concentration $NH_3$ can significantly increase the potential for harmful chlorinated by-product formation.

The applicability of the bilayer-EM for removing low concentration $NO_3^-$ under different electrolyte conditions was further evaluated. Under the single-layer mode at neutral pH, when altering the electrolyte from 10 mM $Na_2SO_4$ to lower ionic strength (1 mM $Na_2SO_4$) and

https://doi.org/10.1038/s41467-025-56102-7

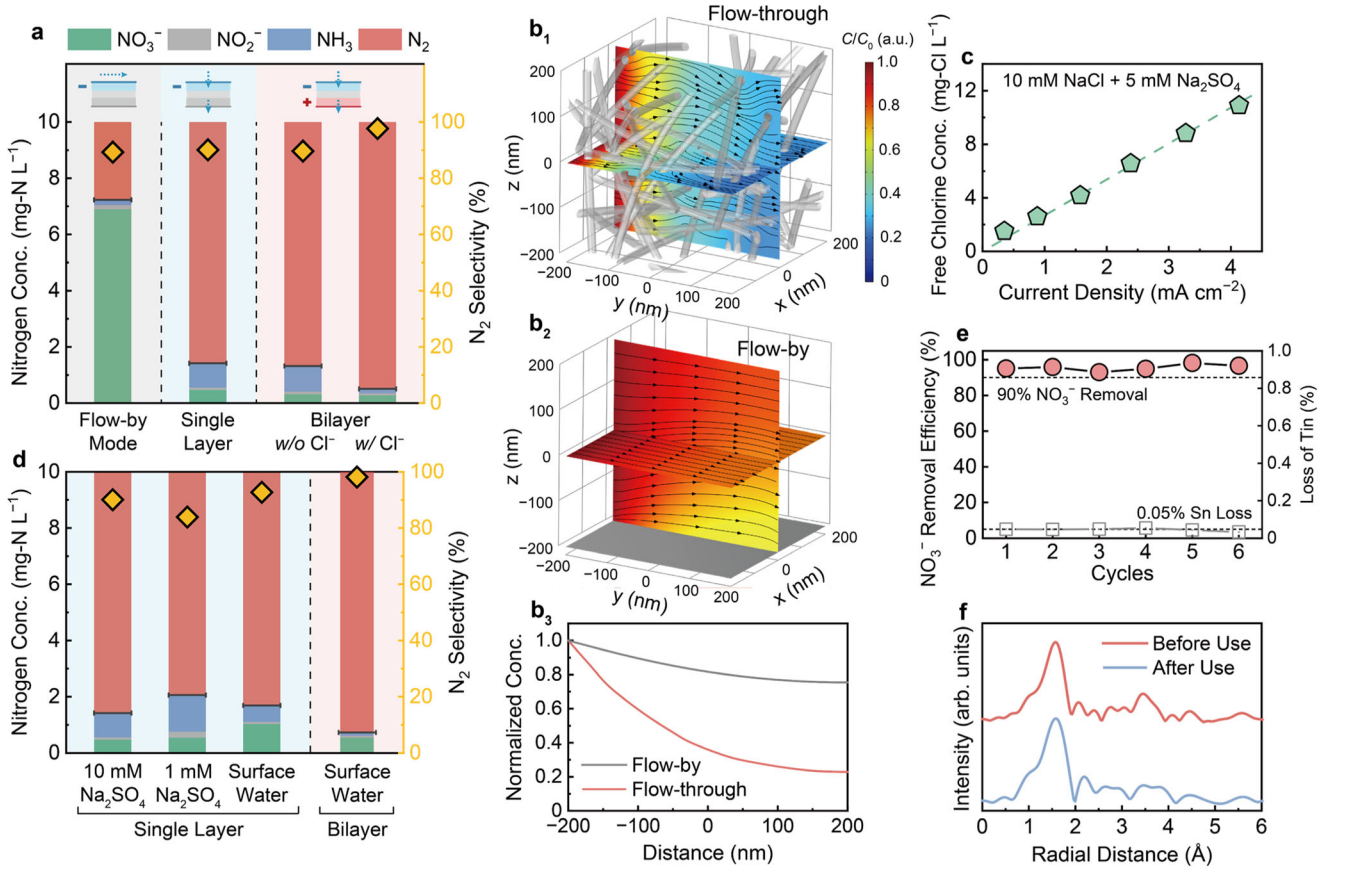


**Fig. 6 | $NO_3RR$ performance and theoretical analysis of the bilayer-EM. a** Effect of electrified operation modes, including flow-by (left, grey shading), single-layer flow-through (middle, blue shading), and bilayer flow-through (right, pink shading) modes, on the distribution of nitrogen species in the permeate (left axis) and $N_2$ selectivity (right axis) using the membrane. Black bars indicate the residual nitrogen concentration (i.e., the sum of $NO_3^-$, $NO_2^-$, and $NH_3$) in the permeate. The voltages were not iR corrected (membrane electrode surface area = 12.6 $cm^2$, resistance value = 23 Ω). CFD simulating the $NO_3^-$ concentration distributions under ($b_1$) flow-through and ($b_2$) flow-by modes and ($b_3$) the concentration changes with flow distance. **c** Generation of free chlorine by the $TiO_{2-x}$-EM as a function of current density using a feed solution with 5 mM $Na_2SO_4$ and 10 mM NaCl under a permeate flow rate of 1.2 mL $min^{-1}$. **d** $NO_3^-$ removal performance of the bilayer-EM when treating different feed solutions containing 10 mg-N $L^{-1}$ $NaNO_3$ in 10 mM $Na_2SO_4$, 1 mM $Na_2SO_4$, or simulated surface water (containing 2 mM $Cl^-$, other constituents listed in Table S2). The data in (**a**) and (**b**) are presented as mean values ± s.d. ($n = 3$). **e** $NO_3^-$ removal efficiency and loss of Sn of the bilayer-EM as a function of filtration cycles. After operating for 1.5 h, the membrane was rinsed and dried and then used for the next cycle. **f** Sn FT-EXAFS spectra of the $Sn_2$/NCB-EM before and after long-term operation. Source data are provided as a Source Data file.

simulated surface water (see Table S2 for the composition), similar $NO_3^-$ removal performances were achieved (Fig. 6d). Under the bilayer mode when treating the simulated surface water, the $N_2$ selectivity further increased to 98.1% as the surface water contained 2 mM $Cl^-$. The simultaneous achievement of high $NO_3^-$ removal efficiency and $N_2$ selectivity of $Sn_2$/NCB bilayer-EM with only ~8 s resident time was superior when compared to the previous $NO_3RR$ system for $NO_3^-$ decontamination to $N_2$ (Table S3). When treating water with $NO_3^-$ concentration at municipal wastewater level of 50 mg-N $L^{-1}$ (Fig. S21), the bilayer-EM also achieved high removal efficiency (86%), conversion rate (2457.6 mg-N $h^{-1}$ $m^{-2}$, a 6-fold enhancement compared to the batch system), and Faradaic efficiency (91%). Notably, the bilayer-EM maintained a stable $NO_3^-$ removal efficiency of ~96% with negligible dissolution of the Sn (<0.05%) throughout a long-term testing (6 repeated cycles which corresponds to 9 h of operation, Fig. 6e). The Sn FT-EXAFS spectra for the $Sn_2$/NCB-EM before and after the long-term operation showed that the Sn maintained the Sn-N coordination structure without aggregation of Sn (Fig. 6f). The Sn XANES spectra for the $Sn_2$/NCB-EM before and after reaction indicated that the oxidation state of Sn was also maintained (Fig. S22). These results collectively demonstrate the high stability of Sn pair-atoms in the flow-through operation, which was ascribed to the strong binding through the nitrogen coordination[61,62]. The robustness of the Sn pair-atom loaded membrane for removing low concentration $NO_3^-$ at realistic water conditions further confirms its superiority over previous nanoparticle-based $NO_3RR$ systems.

## Discussion

In this work, we developed a bilayer electrified membrane incorporating Sn pair-atoms as the $NO_3RR$ catalysts. We successfully demonstrated that the membrane could realize superior removal efficiency and $N_2$ selectivity for converting $NO_3^-$ with low concentrations in single-pass electrofiltration. Our design principles on the catalysts and the electrofiltration system present three major advancements. First, without using noble metals, the Sn pair-atoms enhanced $NO_3^-$ adsorption and electron transfer and promoted *N-*N coupling to result in a high $N_2$ selectivity via facilitating *N spillover, which would be difficult to achieve via fully-isolated single-atom sites. Second, coating the pair-atom catalysts with high $N_2$ selectivity on the interwoven framework of the electrified membrane enhanced the exposure and utilization of the catalysts during flow-through operation to facilitate the $NO_3RR$ compared to directly functionalizing the catalysts on a plate electrode for conventional flow-by operation. Third, the sequential cathode-to-anode $NO_3^-$ reduction and residual $NH_3$ oxidation during the single-pass electrofiltration achieved a near 100% $N_2$ selectivity with near zero total dissolved N in the effluent when treating

water with an low $NO_3^-$ concentration (10 mg-N $L^{-1}$). Further efforts should focus on the mitigation of side reactions when applying electrofiltration to remove contaminants at low concentrations from complex water matrices[63,64]. The findings of this study not only advance the $NO_3RR$ catalyst design but also pave the way for scalable treatment of water containing $NO_3^-$ with low concentrations using electrified membranes.

## Methods

### Chemicals and materials

Tin chloride ($SnCl_4$), tin powder, sodium nitrate ($KNO_3$), 1,10-phenanthroline (1,10-phen), carbon nanotubes (CNT, multi-walled), Nafion solution, isopropanol, N,N-dimethylformamide (DMF), polyacrylonitrile (PAN), and sodium sulfate ($Na_2SO_4$) were purchased from Sigma-Aldrich. Carbon black was obtained from Cabot Corporation (CB, EMPEROR 2000). All chemicals used in the experiments were reagent grade or higher and used as received without further purification. Experimental solutions were prepared using deionized water (DI, >18.2 MΩ·cm) from the Milli-Q system.

### Synthesis of $Sn_2$/NCB and $Sn_1$/NCB

The synthesis step first involved mixing $SnCl_4$ and 1,10-phen at a molar ratio of 1:3 in ethanol. The CB was further added into the mixed solution for impregnation. The nominal loading of Sn was 5% and 1% for $Sn_2$/NCB and $Sn_1$/NCB respectively. The suspensions were dried at 80 °C for 24 h. The catalysts were then calcined at 600 °C for 3 h in a tube furnace (STF1200, Across International) under $N_2$ at a flow rate of 250 sccm.

### Preparation of Sn loaded electrodes

5 mg of $Sn_2$/NCB (or NCB, $Sn_1$/NCB, Sn NC-1%, Sn NC-5%, Sn NP-10%, Sn NP-20%, and Sn metal powder) and 20 μL of 5 wt% Nafion solution were dispersed 1 mL isopropanol, followed by sonication for 1 h to prepare a catalyst ink. 200 μL of the ink was drop-casted on carbon fiber paper with an effective working area of 1 × 1 $cm^2$, giving a mass loading of 1 mg $cm^{-2}$.

### Fabrication of $Sn_2$/NCB-EM

The as-received CNTs were pre-treated in a concentrated HCl solution (36.5–38.0%) at 90 °C under refluxing for 12 h, followed by washing with DI water until neutral and drying at 60 °C for 12 h for preparing the pristine CNTs. A certain amount of $Sn_2$/NCB (10 to 100 mg) and 50 mg of pristine CNTs were dispersed in 40 mL DMF containing 0.1 wt% PAN, followed by sonication for 20 min using an ultrasonic probe. We applied layer-by-layer assembly by vacuum filtering 2 mL of the as-prepared suspension onto a ceramic membrane (0.45 μm, Sterlitech). The prepared membrane with 20 layers in total was then rinsed with DI water followed by drying at 90 °C for 12 h. The $Sn_2$/NCB-FEM was obtained by directly peeling the whole carbonaceous layer off from the ceramic membrane after drying.

### Fabrication of $TiO_{2-x}$-EM

The $TiO_{2-x}$-EM was obtained by calcining a pristine $TiO_2$ membrane (Sterlitech) under pure $H_2$ atmosphere at 1100 °C for 12 h using the tube furnace at a heating rate of 5 °C $min^{-1}$.

### Preparation of bilayer-EM

The bilayer-EM was obtained by stacking the free-standing $Sn_2$/NCB-EM on the $TiO_{2-x}$-EM with a thin macroporous polyester fabric as the spacer in between to separate the membranes.

### Characterizations of catalysts

The Sn loaded onto the catalyst was measured using inductively-coupled plasma mass spectrometry (ICP-MS). The morphology of synthesized $Sn_2$/NCB catalysts was characterized using transmission electron microscopy (TEM, Tecnai Osiris 200 kV, FEI) and aberration-corrected high-angle annular dark-field scanning transmission electron microscopy (AC-HAADF-STEM) at 300 kV. X-ray Diffraction (XRD, Rigaku SmartLab) using Cu Kα radiation ($\lambda$ = 1.542 Å) was carried out to identify the crystallinity of carbon and the existence of metal phases. Raman spectroscopy (LabRAM HR Evolution, Horiba) was carried out to observe the characteristic D and G bands of the catalysts. The Sn 3d and N 1 s were measured by X-ray photoelectron spectroscopy (XPS) with a Versa Probe II scanning XPS microprobe (PhysicalElectronics) using monochromatic Al Kαradiation (1486.6 eV).

### XAFS measurement of $Sn_2$/NCB

To characterize the coordination environment of Sn, X-ray absorption spectra (XAS) at Sn K-edge were recorded at the ISS beamline of the National Synchrotron Light Source II at Brookhaven National Laboratory[65], using a Si(111) double-crystal monochromator and a passivated implanted planar silicon (PIPS) fluorescence detector. Near-edge X-ray absorption spectroscopy (XANES) and extended X-ray absorption fine structure (EXAFS) data were collected at room temperature, with energy calibrated using a Sn foil. EXAFS data was fitted by using Demeter 0.9.25 software package. Athena software was used to calibrate energy and normalize the data. The edge energy was determined using the maximum of the first peak in the first derivative of the XANES spectra[66]. EXAFS spectra were fit using a least-squares fit in R-space of $k^2$ weighted Fourier transform (FT) to determine the coordination number (*CN*) and bond distances (*R*) between Pd and Cu using the Artemis software[66]. The first shell was used to fit the EXAFS spectra. Least-squares fit in R-space of the $k^2$-weighted Fourier transform data from 3.0 to 12.0 $Å^{-1}$ was used to obtain the EXAFS coordination parameters. The amplitude reduction factor ($SO^2$) was determined as 0.78 by fitting a reference spectrum of the Pd foil, and then it was used for fitting all the other EXAFS spectra.

### Characterization of membranes

SEM (SU8230, Hitachi) was employed to investigate the surface and cross-section morphologies of the membrane. Membrane pore size distribution was estimated by analyzing the surface SEM images using Nano Measurer software. Water contact angles were measured by the sessile drop method using a contact angle goniometer (OneAttension, Biolin Scientific). Water flux was calculated by dividing the permeate flow rate by the effective membrane area (i.e., 12.6 $cm^2$). Membrane pore volume was determined by the weight difference between a wet and dry membrane. Water residence time was calculated by dividing the pore volume by the permeate flow rate.

### Electrochemical measurements

Electrochemical measurements were performed by an electrochemical workstation (CHI 660E, CH Instruments) in a typical three-electrode batch cell containing the working electrode, a mixed metal oxide (MMO) electrode as the counter electrode, and an Ag/AgCl electrode as the reference electrode. All potentials were expressed relative to the RHE scale and were calculated using the following equation: E (vs RHE) = E (vs Ag/AgCl) + 0.197 + 0.0591 × pH. LSV curves were collected at a scan rate of 20 mV $s^{-1}$ in 50 mM $Na_2SO_4$ solution with or without 50 mg-N $L^{-1}$ $NaNO_3$ addition. EIS was conducted by applying frequencies ranging from 1 to $10^6$ Hz in a 10 mM $Na_2SO_4$ solution at open circuit voltage. The electrolyte was prepared before each test.

### Batch $NO_3RR$ experiments

The $NO_3^-$ reduction performance of the catalysts was investigated through batch experiments. The batch system consisted of a reactor with the catalyst coated electrode and an MMO mesh electrode with a spacing of 1 cm. Batch experiments were performed for treating 20 mL feed solution with 50 mg-N $L^{-1}$ $NaNO_3$ and 50 mM $Na_2SO_4$ for 2 h at a string rate of 500 rpm. The reason for choosing 50 mg-N $L^{-1}$ instead of

10 mg-N $L^{-1}$ was that the low mass transfer limitations in the batch system would result in no visible effect among different catalysts.

### Electrofiltration $NO_3RR$ experiments

Electrofiltration experiments were performed using a cross-flow membrane filtration system. The membrane and a counter MMO mesh electrode were placed in an electrofiltration cell with 1 cm spacing. Electrolytes containing 10 mg-N $L^{-1}$ $NaNO_3$ in 10 mM $Na_2SO_4$ or in 10 mM NaCl + 5 mM $Na_2SO_4$ at neutral pH were used as the feed solution. The feed was circulated at a flow rate of 200 mL $min^{-1}$ by a peristaltic pump and the permeate flow rate was controlled to 1.2 mL $min^{-1}$.

### Nitrogen speciation and free chlorine measurement

$NO_3^-$, $NO_2^-$, $NH_4^+$, and free chlorine concentrations in both the permeate and the feed were quantified after 1 h of operation. The concentrations of $NO_3^-$, $NO_2^-$, $NH_4^+$, and free chlorine were determined according to the cadmium reduction method, the diazotization method, the Nessler method, and the N,N-diethyl-1,4-phenylenediamine sulfate method respectively, using assay kits (HI93728 for $NO_3^-$, HI93707 for $NO_2^-$, HI93715 for $NH_4^+$, and HI97710 for free chlorine, Hanna Instruments). The standard curves used for the colorimetric quantification of $NO_3^-$, $NO_2^-$ and $NH_4^+$ are shown in Fig. S5. Ion chromatography (IC, 930 Compact, Metrohm) was also employed to double-check the concentrations of the nitrogen ions. The $N_2$ selectivity was calculated by the following equation, where $C$ represents the concentration of a certain ion:

$$N_2\% = \frac{[C_{[NO3-N]_0} - C_{[NO3-N]_t} - C_{[NO2-N]_t} - C_{[NH4-N]_t}]}{C_{[NO3-N]_0} - C_{[NO3-N]_t}} \quad (1)$$

### The Faradaic efficiency (FE) calculation

The FE for the conversion of $NO_3^-$ to $NO_2^-$, $NH_4^+/NH_3$, and $N_2$ were calculated according to the following equation:

$$FE_{NO3RR} = \frac{n \times F \times C_{product} \times V}{MW_{product} \times i \times t} \quad (2)$$

where $n$ is the number of charge equivalents required to produce 1 mole of product ($n = 2$ for $NO_2^-$, $n = 8$ for $NH_4^+/NH_3$, $n = 5$ for $N_2$). $F$ is the Faraday's constant (96485 C/mol), $C_{product}$ is the concentration of product (g/L), $V$ is the volume of the electrolyte (0.04 L), $MW_{product}$ is the molecular weight of products ($MW_{NH3} = 17$ g $mol^{-1}$, $MW_{NO2} = 46$ g $mol^{-1}$, $MW_{N2} = 28$ g $mol^{-1}$), $i$ is the operating current density, and $t$ is the electrolysis time.

### In situ attenuated total reflectance surface-enhanced infrared absorption spectroscopy

ATR-SEIRAS was performed using a Nicolet iS50 FTIR spectrometer equipped with an MCT detector and a reflectance unit for the electrochemical cell at an incidence angle of 60°. The in situ electrochemical cell consisted of two chambers with three electrodes and the chambers were filled with 10 mL of 50 mg-N $L^{-1}$ $NaNO_3$ and 50 mM $Na_2SO_4$ electrolyte. Platinum sheet (1 $cm^2$) and Ag/AgCl were used as the counter electrode and reference electrode, respectively. For the working electrode, 30 µL of catalyst ink (5 mg $mL^{-1}$) was dropped onto a silicon crystal and dried in air before testing. The detector was cooled with liquid nitrogen for at least 30 min before testing to maintain a stable signal. $NO_3RR$ testing was performed using the chronoamperometry method, and the spectral signal was collected after 1 min of reaction. Scans were conducted from the open circuit potential to −1.0 V (vs. RHE). All spectra were given by absorbance with a spectral resolution of 4 $cm^{-1}$ for each curve.

### Density functional theory calculations

Spin-polarized first-principles calculations were performed by using the Perdew-Burke-Ernzerhof (PBE) exchange-correlation functional as implemented in the Vienna ab initio simulation package (VASP). The projector augmented wave (PAW) method and the corresponding pseudopotentials were employed. A cutoff energy of 500 eV was set for the plane wave basis set. The adsorption configurations of $NO_3^-$ on $Sn_1$/NCB and $Sn_2$/NCB and the structures of reaction intermediates were optimized by controlling the convergence thresholds for the energy and force to be $10^{-5}$ eV and 0.02 eV/Å, respectively. During the relaxation, all atomic positions were allowed to relax. The Grimme's DFT-D3 correction method was included to describe the weak dispersion interactions during surface adsorption. A 2 × 2 × 1 Monkhorst-Pack k-point sampling was set for all models. The corresponding adsorption Gibbs free energies were then calculated as

$$\Delta G = \Delta E + \Delta ZPE - T\Delta S \quad (3)$$

where ΔZPE and Δ$S$ are the changes in zero point energy and in entropy, respectively, between the adsorbed state and free state, which can be obtained from the vibrational frequencies calculations (with adsorbates relaxed and substrates fixed) and standard thermodynamic data. $T$ is the temperature. The adsorption energy of species on the surface was calculated as:

$$E_{ads} = E_{x/surface} - E_x - E_{surface} \quad (4)$$

where $E_{x/surface}$, $E_x$, and $E_{surface}$ are the energies of the slab with adsorbed species, the adsorbed species calculated in a cubic cell, and the energies of the slab, respectively.

### Computational fluid dynamics simulation

CFD was performed for flow field simulation inside the membrane using COMSOL Multiphysics software. The geometry was constructed with a cube fluid domain with a side length of 400 nm. The cube was swept with random rotation and movement multiple times to obtain multiple gaps and the geometric structures outside the fluid domain were removed. Three models were built inside the fluid domain, including an interwoven framework with thick fibers, an interwoven framework with thin fibers, and a flat plate control. The simulations were solved based on the Navier-Stokes equations using laminar flow physics. On the basis of the convection velocity calculation, the conservation calculation of convective mass transfer was performed. The calculations meet the dilute species transfer interface under different pore conditions and the mass transfer was simulated through the diffusion equation:

$$\nabla \cdot (-D\nabla c) + \mathbf{u} \cdot \nabla c = R \quad (5)$$

where $D$ is diffusivity ($m^2/s$), $c$ is concentration (mol/$m^3$), $\mathbf{u}$ is fluid velocity vector (m/s), and $R$ is the rate expression of matter (mol/$m^3$·s). Considering that the reaction happens mainly on the surface rather than in the body of the model, the $R$ term here is zero and the overall reaction satisfies Fick's diffusion law. The inlet flow rate at the entrance of the mass transfer region was set to 2.4 µm/s and the surface reaction rate was set to $2 \times 10^{-4}$ m/s as the field boundaries.

## Data availability

All data needed to evaluate the conclusions in the paper are present in the paper and/or the Supplementary Information. Source data are provided with this paper.

## References

1. Spalding, R. F. & Exner, M. E. Occurrence of nitrate in groundwater —a review. *J. Environ. Qual.* **22**, 392–402 (1993).

2. Xu, H., Paerl, H. W., Qin, B., Zhu, G. & Gaoa, G. Nitrogen and phosphorus inputs control phytoplankton growth in eutrophic Lake Taihu, China. *Limnol. Oceanogr.* **55**, 420–432 (2010).
3. Kim, K. et al. Nitrogen stimulates Microcystis-dominated blooms more than phosphorus in river conditions that favor non-nitrogen-fixing genera. *Environ. Sci. Technol.* **54**, 7185–7193 (2020).
4. Duca, M. & Koper, M. T. Powering denitrification: the perspectives of electrocatalytic nitrate reduction. *Energy Environ. Sci.* **5**, 9726–9742 (2012).
5. Xu, H., Ma, Y., Chen, J., Zhang, W.-X. & Yang, J. Electrocatalytic reduction of nitrate–a step towards a sustainable nitrogen cycle. *Chem. Soc. Rev.* **51**, 2710–2758 (2022).
6. Li, J. et al. Atomically dispersed Fe atoms anchored on S and N–codoped carbon for efficient electrochemical denitrification. *Proc. Natl. Acad. Sci.* **118**, e2105628118 (2021).
7. Li, P. et al. A multifunctional copper single-atom electrocatalyst aerogel for smart sensing and producing ammonia from nitrate. *Proc. Natl. Acad. Sci.* **120**, e2305489120 (2023).
8. Wu, Z.-Y. et al. Electrochemical ammonia synthesis via nitrate reduction on Fe single atom catalyst. *Nature Comm* **12**, 2870 (2021).
9. Zhu, T. et al. Single-atom Cu catalysts for enhanced electrocatalytic nitrate reduction with significant alleviation of nitrite production. *Small* **16**, 2004526 (2020).
10. Wang, X. et al. Free-standing membrane incorporating single-atom catalysts for ultrafast electroreduction of low-concentration nitrate. *Proc. Natl. Acad. Sci.* **120**, e2217703120 (2023).
11. Schuytema, G. S. & Nebeker, A. V. Comparative toxicity of ammonium and nitrate compounds to Pacific treefrog and African clawed frog tadpoles. *Environ. Toxicol. Chem.* **18**, 2251–2257 (1999).
12. Gootzen, J. et al. The electrocatalytic reduction of $NO_3^-$ on Pt, Pd and Pt+ Pd electrodes activated with Ge. *J. Electroanal. Chem.* **434**, 171–183 (1997).
13. Kato, M., Okui, M., Taguchi, S. & Yagi, I. Electrocatalytic nitrate reduction on well-defined surfaces of tin-modified platinum, palladium and platinum-palladium single crystalline electrodes in acidic and neutral media. *J. Electroanal. Chem.* **800**, 46–53 (2017).
14. Wang, Y., Wang, C., Li, M., Yu, Y. & Zhang, B. Nitrate electroreduction: mechanism insight, in situ characterization, performance evaluation, and challenges. *Chem. Soc. Rev.* **50**, 6720–6733 (2021).
15. Yang, X.-F. et al. Single-atom catalysts: a new frontier in heterogeneous catalysis. *Acc. Chem. Res.* **46**, 1740–1748 (2013).
16. Li, J. et al. Highly active and stable metal single-atom catalysts achieved by strong electronic metal–support interactions. *J. Am. Chem. Soc.* **141**, 14515–14519 (2019).
17. Zhuo, H.-Y. et al. Theoretical understandings of graphene-based metal single-atom catalysts: stability and catalytic performance. *Chem. Rev.* **120**, 12315–12341 (2020).
18. Liu, J. Catalysis by supported single metal atoms. *ACS Catal* **7**, 34–59 (2017).
19. Murphy, E. et al. Elucidating electrochemical nitrate and nitrite reduction over atomically-dispersed transition metal sites. *Nature Comm* **14**, 4554 (2023).
20. Wang, S. et al. High-throughput identification of highly active and selective single-atom catalysts for electrochemical ammonia synthesis through nitrate reduction. *Nano Energy* **100**, 107517 (2022).
21. Xue, Y. et al. Electrocatalytic hydrogenation boosts reduction of nitrate to ammonia over single-atom Cu with Cu(I)-$N_3C_1$ sites. *Environ. Sci. Technol.* **56**, 14797–14807 (2022).
22. Yin, H., Peng, Y. & Li, J. Electrocatalytic reduction of nitrate to ammonia via a Au/Cu single atom alloy catalyst. *Environ. Sci. Technol.* **57**, 3134–3144 (2023).
23. Cheng, X. F. et al. Coordination symmetry breaking of single-atom catalysts for robust and efficient nitrate electroreduction to ammonia. *Adv. Mater.* **34**, 2205767 (2022).
24. Li, J. et al. Boosted ammonium production by single cobalt atom catalysts with high Faradic efficiencies. *Proc. Natl. Acad. Sci.* **119**, e2123450119 (2022).
25. Liu, H. et al. Efficient electrochemical nitrate reduction to ammonia with copper-supported rhodium cluster and single-atom catalysts. *Angew. Chem. Inter. Edit.* **61**, e202202556 (2022).
26. Li, R. & Wang, D. Superiority of dual-atom catalysts in electrocatalysis: one step further than single-atom catalysts. *Adv. Ener. Mater.* **12**, 2103564 (2022).
27. Fajardo, A. S., Westerhoff, P., Sánchez-Sánchez, C. M. & Garcia-Segura, S. Earth-abundant elements a sustainable solution for electrocatalytic reduction of nitrate. *Appl. Catal. B Environ.* **281**, 119465 (2021).
28. Garcia-Segura, S., Lanzarini-Lopes, M., Hristovski, K. & Westerhoff, P. Electrocatalytic reduction of nitrate: Fundamentals to full-scale water treatment applications. *Appl. Catal. B Environ.* **236**, 546–568 (2018).
29. Ma, W. et al. Catalytic membrane with copper single-atom catalysts for effective hydrogen peroxide activation and pollutant destruction. *Environ. Sci. Technol.* **56**, 8733–8745 (2022).
30. Meng, C. et al. Angstrom-confined catalytic water purification within Co-TiOx laminar membrane nanochannels. *Nature Comm* **13**, 4010 (2022).
31. Wu, X. et al. Single-atom cobalt incorporated in a 2D graphene oxide membrane for catalytic pollutant degradation. *Environ. Sci. Technol.* **56**, 1341–1351 (2021).
32. Zuo, K. et al. Electrified water treatment: fundamentals and roles of electrode materials. *Nature Rev. Mater.* **8**, 472–490 (2023).
33. Sun, M. et al. Electrified membranes for water treatment applications. *ACS EST Engg* **1**, 725–752 (2021).
34. Zhao, Y. et al. Emerging challenges and opportunities for electrified membranes to enhance water treatment. *Environ. Sci. Technol.* **56**, 3832–3835 (2022).
35. Gayen, P. et al. Electrocatalytic reduction of nitrate using magnéli phase $TiO_2$ reactive electrochemical membranes doped with Pd-based catalysts. *Environ. Sci. Technol.* **52**, 9370–9379 (2018).
36. Li, Y., Ma, J., Waite, T. D., Hoffmann, M. R. & Wang, Z. Development of a mechanically flexible 2D-MXene membrane cathode for selective electrochemical reduction of nitrate to $N_2$: mechanisms and implications. *Environ. Sci. Technol.* **55**, 10695–10703 (2021).
37. Ma, J. et al. Electrochemical reduction of nitrate in a catalytic carbon membrane nano-reactor. *Water Res.* **208**, 117862 (2022).
38. Yang, H. et al. A universal ligand mediated method for large scale synthesis of transition metal single atom catalysts. *Nat. Commun.* **10**, 4585 (2019).
39. Accorsi, G., Listorti, A., Yoosaf, K. & Armaroli, N. 1, 10-Phenanthrolines: versatile building blocks for luminescent molecules, materials and metal complexes. *Chem. Soc. Rev.* **38**, 1690–1700 (2009).
40. Fox, G. A., Bhattacharya, S. & Pierpont, C. G. Structural and electrochemical properties of binuclear complexes containing 1, 10-phenanthroline-5, 6-diolate as a bridging ligand. *Inorg. Chem.* **30**, 2895–2899 (1991).
41. Wang, Y. Y., Wang, X., Shi, Q. Z. & Gao, Y. C. A novel binuclear copper (II) complex with fumarate and 1, 10-phenanthroline. *Transit. Met. Chem.* **27**, 481–484 (2002).
42. Chai, Y. et al. Dual-atom catalyst with N-colligated $Zn_1Co_1$ species as dominant active sites for propane dehydrogenation. *J. Am. Chem. Soc.* **146**, 263–273 (2023).
43. Shan, J. et al. Metal-metal interactions in correlated single-atom catalysts. *Sci. Adv.* **8**, eabo0762 (2022).
44. Zhang, Y.-X. et al. General synthesis of a diatomic catalyst library via a macrocyclic precursor-mediated approach. *J. Am. Chem. Soc.* **145**, 4819–4827 (2023).

45. Zhao, X. et al. Highly efficient electrochemical $CO_2$ reduction on a precise homonuclear diatomic Fe–Fe catalyst. *ACS Catal.* **12**, 11412–11420 (2022).
46. Reddy, A. L. M. et al. Synthesis of nitrogen-doped graphene films for lithium battery application. *ACS Nano* **4**, 6337–6342 (2010).
47. Zhu, H. et al. Ni–M–O (M= Sn, Ti, W) catalysts prepared by a dry mixing method for oxidative dehydrogenation of ethane. *ACS Catal.* **6**, 2852–2866 (2016).
48. Guo, J. et al. Control over electrochemical $CO_2$ reduction selectivity by coordination engineering of tin single-atom catalysts. *Adv. Sci.* **8**, 2102884 (2021).
49. Maurer, F. et al. Tracking the formation, fate and consequence for catalytic activity of Pt single sites on $CeO_2$. *Nat. Catal.* **3**, 824–833 (2020).
50. Guo, Y., Wang, M., Zhu, Q., Xiao, D. & Ma, D. Ensemble effect for single-atom, small cluster and nanoparticle catalysts. *Nat. Catal.* **5**, 766–776 (2022).
51. Cheng, X. et al. Unveiling structural evolution of Fe single atom catalyst in nitrate reduction for enhanced electrocatalytic ammonia synthesis. *Nano Res.* **17**, 6826–6832 (2024).
52. Liu, Y. et al. Shear-strained Pd single-atom electrocatalysts for nitrate reduction to ammonia. *Angew. Chem. Inter. Edit.* **63**, e202411396 (2024).
53. Zhang, S. et al. Oxygen-coordinated single Mn sites for efficient electrocatalytic nitrate reduction to ammonia. *Nano-Micro Lett.* **16**, 9 (2024).
54. Clarke, O. J., Rowley, A., Fox, R. V., Atifi, A. & Burgess, I. J. Diamonds in the rough: direct surface enhanced infrared spectroscopic evidence of nitrogen reduction on boron-doped diamond supported metal catalysts. *Anal. Chem.* **95**, 10476–10480 (2023).
55. Li, T. et al. A spectroscopic study on nitrogen electrooxidation to nitrate. *Angew. Chem. Inter. Edit.* **135**, e202217411 (2023).
56. Li, X. et al. Unique two-electron transfer pathway of Bismuth nanocrystal for enhanced $N_2$ electroreduction revealed by in situ infrared spectroscopy. *Appl. Catal. B Environ.* **342**, 123365 (2024).
57. Liu, Z. et al. Electrochemically mediated nitrate reduction on nanoconfined zerovalent iron: properties and mechanism. *Water Res.* **173**, 115596 (2020).
58. Zhang, C., He, D., Ma, J. & Waite, T. D. Active chlorine mediated ammonia oxidation revisited: Reaction mechanism, kinetic modelling and implications. *Water Res.* **145**, 220–230 (2018).
59. Huo, Z.-Y. et al. Synergistic nanowire-enhanced electroporation and electrochlorination for highly efficient water disinfection. *Environ. Sci. Technol.* **56**, 10925–10934 (2022).
60. Li, Q., Liu, G.-h, Qi, L., Wang, H. & Xian, G. Chlorine-mediated electrochemical advanced oxidation process for ammonia removal: Mechanisms, characteristics and expectation. *Sci. Total Environ.* **896**, 165169 (2023).
61. Chen, C. et al. Local reaction environment in electrocatalysis. *Chem. Soc. Rev.* **53**, 2022–2055 (2024).
62. Zhang, Y. et al. The effect of coordination environment on the activity and selectivity of single-atom catalysts. *Coord. Chem. Rev.* **461**, 214493 (2022).
63. Alkhadra, M. A. et al. Electrochemical methods for water purification, ion separations, and energy conversion. *Chem. Rev.* **122**, 13547–13635 (2022).
64. Gao, X. et al. Boosting urea electrooxidation on oxyanion-engineered nickel sites via inhibited water oxidation. *Nat. Commun.* **14**, 5842 (2023).
65. Leshchev, D. et al. The Inner Shell Spectroscopy beamline at NSLS-II: a facility for in situ and operando X-ray absorption spectroscopy for materials research. *J. Synchrotron Radiat.* **29**, 1095–1106 (2022).
66. Ravel, B. & Newville, M. ATHENA, ARTEMIS, HEPHAESTUS: data analysis for X-ray absorption spectroscopy using IFEFFIT. *J. Synchrotron Radiat.* **12**, 537–541 (2005).


## Acknowledgements

This study was supported by National Natural Science Foundation of China (nos. 52470044 and 52400098), NSF Division of Chemical, Bioengineering, Environmental, and Transport Systems (CBET) Grant #1955793, the NSF Nanosystems Engineering Research Center for Nanotechnology-Enabled Water Treatment (ERC-1449500), Guangdong Basic and Applied Basic Research Foundation (2024A1515012461), Shenzhen Key Laboratory of Advanced Technology for Marine Ecology (ZDSYS20230626091459009). We acknowledge Dr. Qingxiao Wang at the Imaging and Characterization Core Lab at King Abdullah University of Science and Technology for his assistance in HAADF-STEM measurements. This research used ISS beamline (8-ID) of the National Synchrotron Light Source II, a U.S. Department of Energy (DOE) Office of Science User Facility operated for the DOE Office of Science by Brookhaven National Laboratory under Contract No. DE-SC0012704.

## Author contributions

X. Wu, X. Wang, and J.-H. K. designed research; X. Wu and X. Wang performed research; Y. Wu, H. X., Z. L., R. H., and K. R. analyzed data; X. Wu, X. Wang, Z. W., and J.-H. K wrote the paper.

## Competing interests

The authors declare no competing interests.

## Additional information

**Supplementary information** The online version contains supplementary material available at https://doi.org/10.1038/s41467-025-56102-7.

**Correspondence** and requests for materials should be addressed to Xiaoxiong Wang or Jae-Hong Kim.

**Peer review information** *Nature Communications* thanks Dong-Hee Lim, and the other, anonymous, reviewer(s) for their contribution to the peer review of this work. A peer review file is available.